applied sciences

MDPI

Article

A Low-Profile Dual-Polarized Transmitarray with Enhanced Gain and Beam Steering at Ku Band

Md. Imran Khan [1], Antonella Maria Loconsole [1], Francesco Anelli [1], Vito Vincenzo Francione [1], Ahsan Ullah Khan [2], Marco Simone [2], Gino Sorbello [2] and Francesco Prudenzano [1,*]

[1] Department of Electrical and Information Engineering, Politecnico di Bari, 70126 Bari, Italy; m.khan7@phd.poliba.it (M.I.K.); antonellamaria.loconsole@poliba.it (A.M.L.); francesco.anelli@poliba.it (F.A.); v.francione@phd.poliba.it (V.V.F.)

[2] Department of Electrical, Electronics and Computer Engineering, University of Catania, 95124 Catania, Italy; ahsan.khan@phd.unict.it (A.U.K.); marco.simone@unict.it (M.S.); gino.sorbello@unict.it (G.S.)

* Correspondence: francesco.prudenzano@poliba.it

Abstract: A low profile dual polarized transmitarray antenna, made of three identical layers, is proposed in this paper for Ku-band applications. The transmitarray comprises 22 × 22 symmetrical unit cells. A 3-bit phase compensation layer with less than α_T = 1.3 dB transmission loss and 2π transmission phase coverage for both linear polarized components at the central frequency f_0 = 12 GHz is designed. Moreover, for an incidence angle $\theta = 30^\circ$, the unit cell transmission loss is less than 2 dB; the transmission phase is close to the transmission phase at zero incidence angle $\theta = 0^\circ$. The fabricated transmitarray exhibits a measured peak gain of Gm_0 = 21 dB at the frequency f_0 = 12 GHz. The corresponding measured 1 dB gain bandwidth is BWg = 10.8% (11.1–12.4 GHz). The measured peak side lobe levels are $SLL_0 = -20.8$ dB at f_0 = 12 GHz. The transmitarray antenna can be used for beam steering up to an angle of $\gamma_{max} = \pm 30^\circ$ with a measured scan loss $\triangle G_{MSL1}$ = 2.73 dB at f_1 = 12.4 GHz.

Keywords: low profile; dual polarized; transmitarray antenna; 3-bit phase compensation; beam steering

Academic Editor: Alexander Barkalov

Received: 25 March 2025
Revised: 18 April 2025
Accepted: 19 April 2025
Published: 23 April 2025

Citation: Khan, M.I.; Loconsole, A.M.; Anelli, F.; Francione, V.V.; Khan, A.U.; Simone, M.; Sorbello, G.; Prudenzano, F. A Low-Profile Dual-Polarized Transmitarray with Enhanced Gain and Beam Steering at Ku Band. *Appl. Sci.* **2025**, *15*, 4656. https://doi.org/10.3390/app15094656

1. Introduction

Modern high frequency wireless networks require highly directive antennas to leverage beam forming and beam steering to enhance the information channel capacity. These types of antennas are hugely used in satellite systems, wireless power transmission, and 5G networks. The suitability of phased array antennas in different application areas is well known but require complex feed networks [1–7]. In high-gain applications, significant losses are common because the complexity and insertion loss in the feed network increase with the number of radiating elements. Additionally, losses and costs are increased due to the employment of numerous phase shifters. To overcome this problem, transmitarray antennas are proposed in several studies as a promising alternative to conventional phased array antennas [8–16]. A transmitarray (TA) generally consists of a single feed antenna and a metasurface capable of controlling the phase and amplitude of the feed signal. A TA system can be used for effective beam forming if it consists of a metasurface which has the capability of low loss transmission with a control of 360° transmission phase. A metasurface can be equipped with components such as varactors, diodes, MEMS, and liquid crystals (LC) for the purpose of beam steering in a desired direction, though these active elements increase fabrication complexity and losses [17–20]. On the other hand,

moving the position of the feed source also leads to beam steering [21–23]. The performance of the TA depends on two essential factors, the size of the metasurface (D) and the focal distance (F) of the metasurface. The ratio F/D influences the power transfer to the metasurface [24]. As a result, the spillover and taper efficiency product depend on the F/D ratio. The increase of focal distance (F) causes an enhancement of taper efficiency but a decay in spillover efficiency, whereas enlargement of the size of the metasurface (D) improves the spillover efficiency but makes the metasurface less compact. Low-profile beam-steering TA antennas can be designed using a phase gradient metasurface. For instance, low-profile beam-steering TAs for 5G mm-wave communication were developed with multiple feed horn antennas in [25–29].

Another important feature of next-generation wireless communication systems is the dual-polarized operation which increases the reliability of the radio link and enhances the overall system capacity. Continuous phase tuning, dual-polarized TAs have been reported in the recent literature, via dual-frequency selective surface layers [30–34], the cascade of three metallic layers [35–38], and quantized phase compensation [39–43].

This paper proposes a novel monolithic unit cell design that achieves low profile, dual-polarized operation, and 3-bit phase compensation with minimal transmission loss, allowing to obtain performance comparable with the state of the art in terms of gain, side lobe levels, and scan loss. These results are reached with a novel symmetrical geometry, making it intrinsically suitable for dual polarized radiation. An equivalent circuit model (ECM) of the proposed UC is then developed and the scattering parameters derived from that model are simulated, showing a good match with full-3D numerical simulated results. Based on the developed UC, a proof-of-principle test TA is designed and fabricated, its characterization confirming the expected gain and side lobe levels. Moreover, the developed TA also enables efficient beam steering over tens of angular degrees with minimal scan loss, demonstrating its potential for advanced beam-forming applications.

The paper is organized as follows: after the Introduction, Section 2 describes the UC design and its simulated performance. Section 3 presents the ECM of the UC and compares the corresponding scattering parameters with those calculated via the full-3D numerical simulation. Section 4 outlines the design procedure of the TA antenna, whereas Section 5 shows the comparison between the full wave simulated numerical model of the transmit array and the experimental results. Finally, Section 6 compares the performance of the proposed TA with recent research works, while Section 7 is for concluding remarks.

2. UC Design

The top and side view of the proposed UC is illustrated in Figure 1, the green color representing the substrate and the yellow color the metal. Three identical layers constitute the UC optimized for the phase compensation of the feed incident beam. A symmetric geometry is chosen to allow the dual polarization operation. The metal layer consists of a metal ring, with an outer radius R_1 and inner radius R_2, and an inner circle of radius R_3.

In the design, the ranges for searching for the optimized dimensions are listed in Table 1. They are defined after the preliminary simulations. Eight UCs are designed by changing the values of R_1, R_2, and R_3 to achieve 3-bit phase with low transmission loss. The specific dimensions of the eight UCs are listed in Table 2 with the corresponding transmission magnitude and phase. The substrate used is Rogers RT/duroid 5880 (ε_r = 2.2, tanδ = 0.0009). The thickness of the substrate is t = 1.575 mm ($0.063\lambda_0$). The metal thickness is 35 µm. The periodicity of the UC is P = 8.65 mm ($0.346\lambda_0$), λ_0 = 25 mm being the central wavelength at the frequency f_0 = 12 GHz.

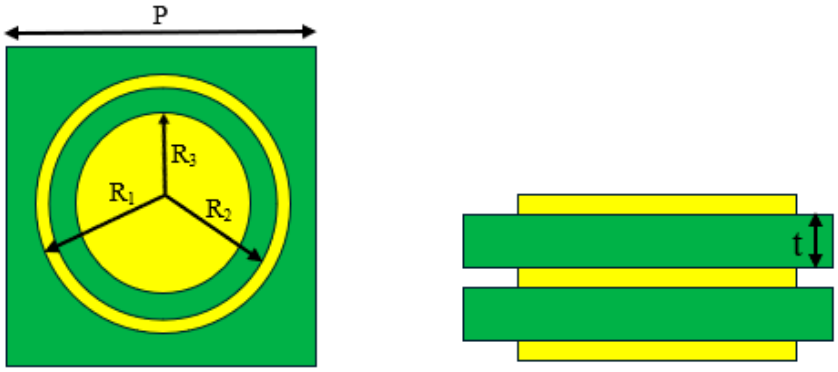

(**a**) (**b**)

Figure 1. (**a**) Top and (**b**) side views of proposed monolithic UC, consisting of three identical metal layers. Yellow part represents metal, and green part is substrate.

Table 1. Range for geometrical parameter optimization.

Parameters	Value (mm)
P	8.65
R_1	3.8–4.325
R_2	3.7–4.225
R_3	2.55–4.11
T	1.575

Table 2. Geometrical dimensions for 3-bit phases and corresponding magnitudes.

UC No.	R_1 (mm)	R_2 (mm)	R_3 (mm)	$\lvert S_{2,1} \rvert$ (dB)	$\angle S_{2,1}$ (deg)
1	4.325	4.225	4.11	−0.86	46
2	4.325	4.225	4.07	−0.58	89
3	4.325	4.225	3.96	−0.92	136
4	4.20	4.10	3.83	−0.20	179.3
5	4.25	4.15	3.60	−0.71	225
6	4.325	4.20	3.07	−1.23	270.6
7	4.20	4.10	2.63	−0.17	314
8	3.80	3.70	2.55	−1.16	359.6

The electric field of an incident wave on the UC with arbitrary linear polarization can be expressed by Equation (1) [44]:

$$\overline{E}_{inc} = E_x\overline{x} + E_y\overline{y} \quad (1)$$

where E_x and E_y are the incident electric field components along the orthogonal linear polarizations. Each UC can be modeled as a 2 × 2 transmission matrix relating to input and output fields found in literature [44]:

$$\begin{pmatrix} \overline{E}_{x,out} \\ \overline{E}_{y,out} \end{pmatrix} = \begin{pmatrix} T_{xx} & T_{xy} \\ T_{yx} & T_{yy} \end{pmatrix} \begin{pmatrix} \overline{E}_{x,in} \\ \overline{E}_{y,in} \end{pmatrix} \quad (2)$$

where T_{xx}, T_{yy} and T_{xy}, T_{yx} are the co-polar and cross-polar transmission coefficients, respectively. If the off-diagonal terms T_{xy}, T_{yx} are null terms, then dual-polarized operation can be expected. Thus, for dual-polarized operation, the transmission matrix T is [44]:

$$T = \begin{pmatrix} |T_{xx}|e^{j\angle T_{xx}} & 0 \\ 0 & |T_{yy}|e^{j\angle T_{yy}} \end{pmatrix} \quad (3)$$

where $\angle T_{xx}$ and $\angle T_{yy}$ are the phase shifts applied to x- and y-polarized waves respectively.

The CST Studio suite software (2023 version) is employed to simulate the magnitude (T_{xx} and T_{yy}), and the phase ($\angle T_{xx}$ and $\angle T_{yy}$), of the transmission coefficient for co-polarized signal components xx or yy, respectively, for each of the eight UCs. These transmission coefficients correspond to the scattering parameter magnitude $|S_{2,1}|$ and phase $\angle S_{2,1}$ between ports 1 and 2, respectively. Moreover, due to symmetry, the x- and y-polarized transmission coefficients are identical. UC boundary conditions are applied in Floquet port configuration, along the x and y directions, as illustrated in Figure 2, to simulate an infinite array. The open boundaries are imposed along the z direction. The Floquet ports along the *z*-axis are used for exciting plane waves.

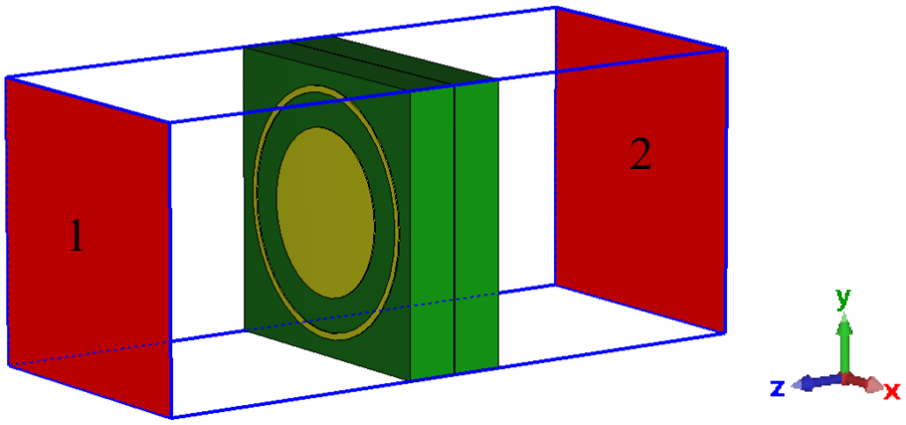

Figure 2. UC simulation by assigning Floquet ports.

The obtained results for the different UC_i are plotted in Figure 3a. The highest transmission loss, obtained at the frequency f_0 = 12 GHz, is α_T = 1.23 dB, corresponding to UC_6. From Figure 3b, it can be observed that, at the frequency f_0, eight UCs cover the 3-bit phases required for co-polarized components. Moreover, in the TA design, it is important to investigate the performance of the UC for different incidence angles θ. For this purpose, the transmission magnitude and phase for the co-polarized components are simulated for different incidence angles θ. Figure 4a shows the transmission loss α_T for co-polarized components is less than 1.9 dB at for an incidence angle θ = 30°. Figure 4b illustrates the transmission phases $\angle T_{xx}$ and $\angle T_{yy}$ of co-polarized components at f_0 = 12 GHz. For θ = 30°, the transmission phase is close to the value obtained at θ = 0° with a maximum simulated displacement of about △P = 20°. In all cases, the UCs will transmit the incidence ray in the proper direction with low transmission loss. The behavior of these UCs for cross-polarized components xy, yx is also investigated. The transmission magnitude T_{xy} and T_{yx} as a function of the frequency f for the cross-polarized components of these UCs are plotted in Figure 5. The highest transmission magnitude value among all these cross-polarized components is $T_{max} = -51$ dB which is very low.

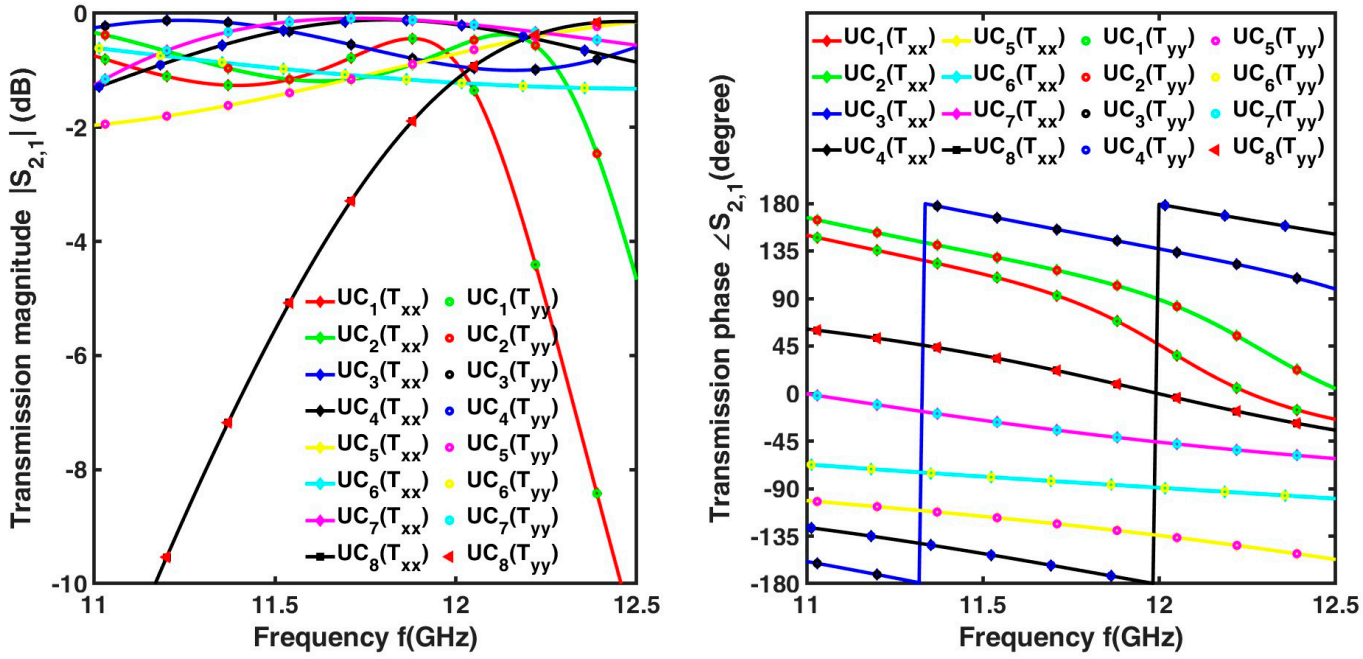

(**a**) (**b**)

Figure 3. (**a**) Transmission magnitude $|S_{2,1}|$ as a function of the frequency f for co-polarized components; (**b**) Transmission phase $\angle S_{2,1}$ as a function of the frequency f for co-polarized components.

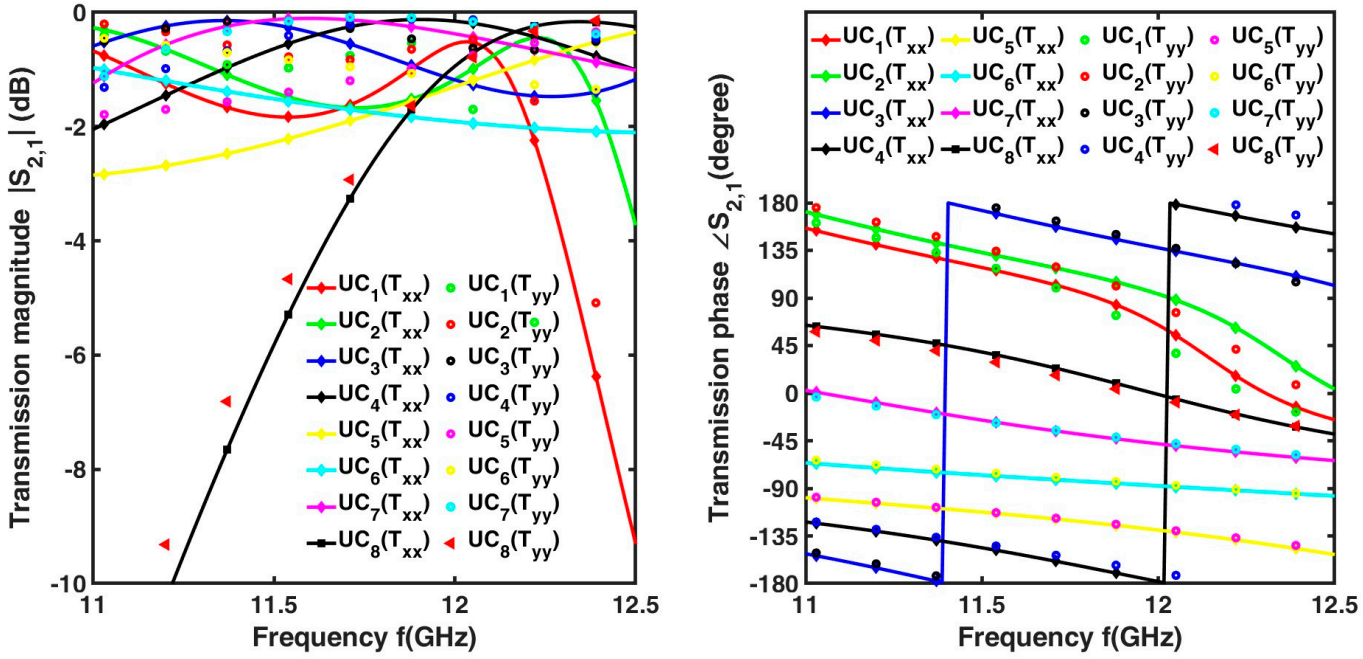

(**a**) (**b**)

Figure 4. (**a**) Transmission magnitude $|S_{2,1}|$ as a function of frequency f for co-polarized components for $\theta = 30°$; (**b**) Transmission phase $\angle S_{2,1}$ as a function of frequency f for co-polarized components for $\theta = 30°$.

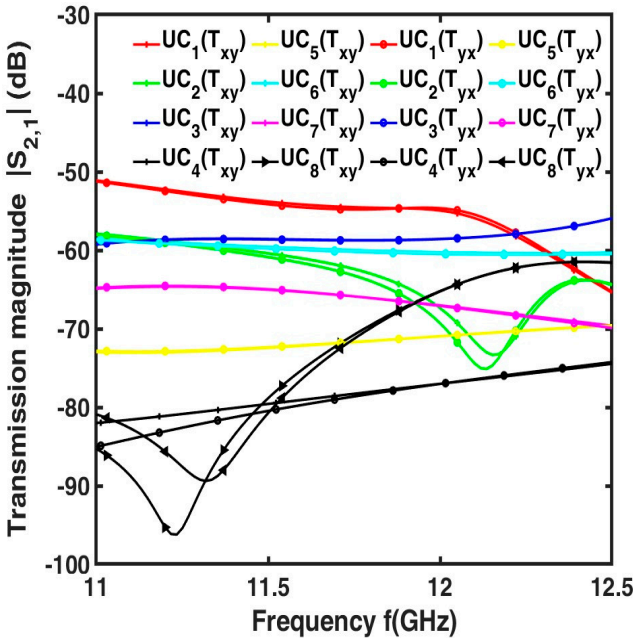

Figure 5. Transmission magnitude $|S_{2,1}|$ as a function of frequency f for cross-polarized components.

3. Equivalent Circuit Analysis of the UC

The ECM of the UC was developed using the same principle followed in the literature [45] for a better understanding of its operation. Then, it was simulated with Advanced Design System (ADS) software (2023 version). The simulated S parameter values of ADS software (2023 version) were compared with those obtained by the CST simulation. Figure 6 shows two adjacent UCs and the ECM. Starting from the UC geometry, the inductive and the capacitive behavior of the different parts of the metallic pattern are represented by means of discrete component as capacitors or inductors. In particular, the inductances of the inner circular metal portion and the outer ring are modeled by inductors L_c and L_r, respectively. The gap between the metal circle and the outer ring is represented by a capacitor C_g. The capacitance formed between the metallic circles of two adjacent cells is represented by C_1. Similarly, the capacitance formed between the outer metal rings of two adjacent cells is represented by C_0. The substrate is modelled using transmission line theory. It is modeled as a transmission line having an impedance of $Z_S = Z_0/\sqrt{\varepsilon_r} = 255\ \Omega$, where $Z_0 = 377\ \Omega$ is the characteristic impedance of free space and $\varepsilon_r = 2.2$ is the relative permittivity of the substrate.

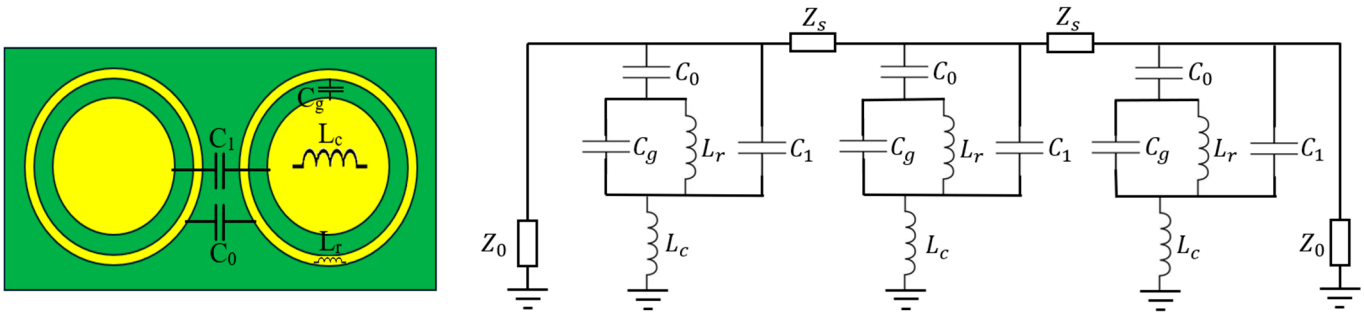

(**a**) (**b**)

Figure 6. (**a**) Top layer of two adjacent UCs and (**b**) ECM of a single UC.

Z_s is the substrate impedance and Z_0 represents the characteristic impedance of free space. The value of the capacitances and inductances are the same for all three metal layers.

UC_6 is chosen for computing the circuit component values of ECM. For UC_6, providing $\angle S_{2,1} = 270°$ transmission, the outer radius of the metal ring, the inner radius of the metal ring, and the radius of the inner circle, are $R_1 = 4.325$ mm, $R_2 = 4.20$ mm, and $R_3 = 3.07$ mm respectively. The circuit component values of the ECM for UC_6 are listed in Table 3. These values are computed using gradient-based optimization method by ADS software. The target of this optimization is to obtain the same magnitude $|S_{2,1}|$, and phase $\angle S_{2,1}$ values of the scattering parameters at the corresponding frequencies f found in CST simulation by tuning the values of the circuit components. The transmission phases of the UC are mainly dependent on the values of the capacitors and the inductors. Figure 7 shows the magnitude and phase values of scattering parameter $S_{2,1}$ of UC_6 for both CST simulation and ECM calculation. A good agreement is reached.

Table 3. Values of circuit components of UC_6 ECM.

Parameters	Value
C_0	0.323 pF
C_g	0.042 pF
C_1	0.019 pF
L_r	3.727 nH
L_c	1.729 nH

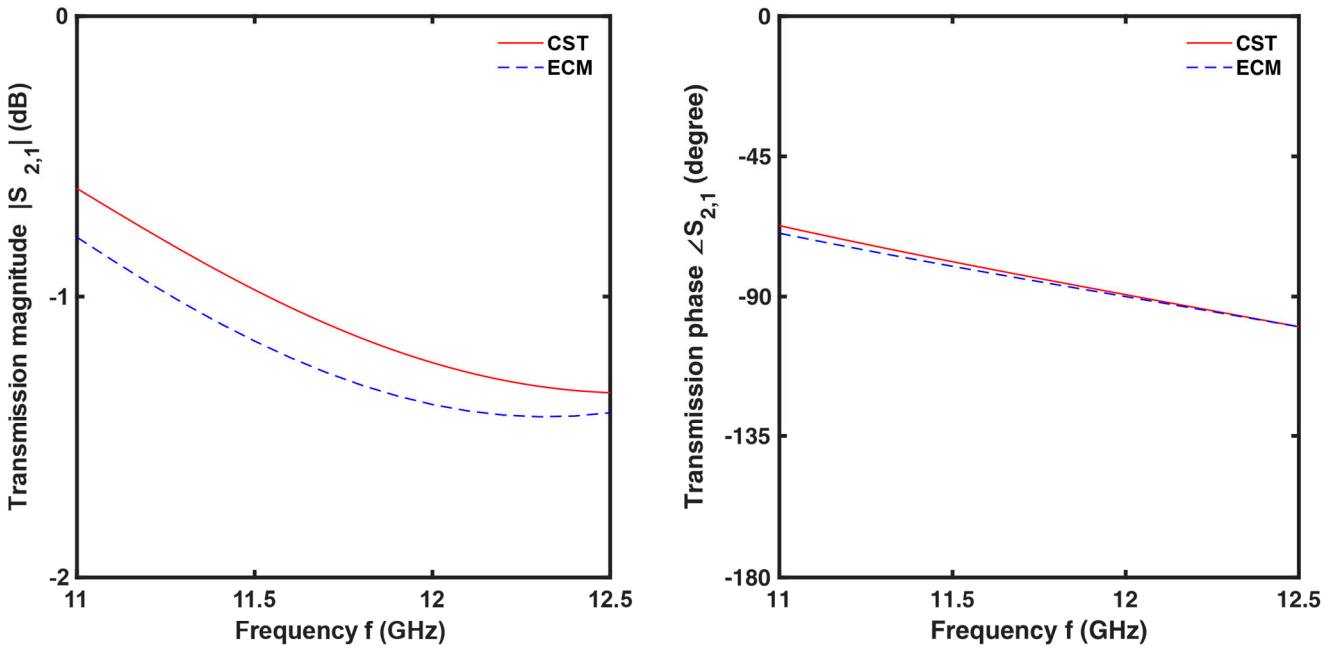

Figure 7. Transmission magnitude $|S_{2,1}|$ and transmission phase $\angle S_{2,1}$ of UC_6 as a function of frequency f, obtained by CST and ECM simulation. (**a**) Transmission magnitude; (**b**) transmission phase.

4. The TA Antenna

In this work, a focal length-to-diameter ratio (F/D) of 0.6 was chosen, and a maximum D size of 200 mm was considered. Based on this requirement, a suitable feed antenna was selected: in particular, a substrate integrated waveguide (SIW)-based 2 × 2 array antenna [46] was used, as shown in Figure 8. This feed antenna array consists of two Rogers RT/duroid 5880 substrates ($\varepsilon_r = 2.2$, $\tan\delta = 0.0009$). The thickness of the first substrate is $T_1 = 0.381$ mm, and for the second is $T_2 = 1.575$ mm. The length and width of the substrates are L = 35 mm, W = 35 mm, respectively. The diameters of the vias connecting both grounds and the diame-

ter of the circular slot in the first ground are D_1 = 0.62 mm and D_2 = 15.05 mm, respectively. The patch width, length are P_1 = 7.7 mm, P_2 = 7.7 mm, and the dimensions regarding lateral and corner slot in the patch are P_3 = 2.75 mm, P_4 = 1.44 mm, and P_5 = 2.18 mm, respectively shown in Figure 8. Specifically, the 2 × 2 array in [46] is chosen because it has a −10 dB beamwidth of approximately 66°, which aligns with the chosen F/D ratio and the target D size. This feed antenna supports a bandwidth of BW = 2.5 GHz (10–12.5 GHz) with an impedance bandwidth of BW_z = 20.83%, having a peak gain G_{f0} = 12.93 dB and G_{f1} = 12.83 dB at f_0 = 12 GHz and f_1 = 12.4 GHz, respectively [46].

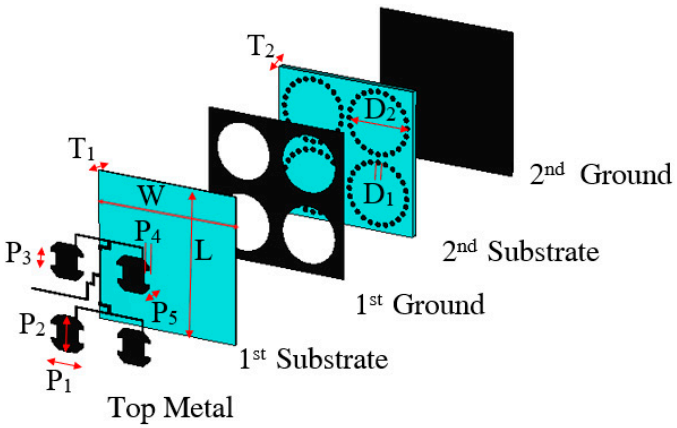

Figure 8. Feed antenna array stack up with dimensions (P_1 = 7.70 mm, P_2 = 7.70 mm, P_3 = 2.75 mm, P_4 = 1.44 mm, P_5 = 2.18 mm, D_1 = 0.62 mm, D_2 = 15.05 mm, T_1 = 0.381 mm, T_2 = 1.575 mm, L = 35 mm, W = 35 mm); metal portion and substrate 1 and 2 are represented by black and blue colors, respectively.

A 22 × 22 sized TA is designed and implemented using the proposed UC. As a result of this design approach, the width of the TA is D = 22 × 8.65 mm = 190.3 mm and the focal distance is F = 0.6 × D = 114.18 mm. The transmission phase of the UC of the TA needs to be adjusted to steer the beam in the desired direction. The phase adjustment of the UC compensates the spatial phase delay, which is introduced due to the distance, d_p, between the feed antenna and the corresponding pth UC (see also Figure 9a). For optimal beam forming in the targeted direction, (θ_0, φ_0), the required phase shift across the TA is computed as follows. The phase of the transmitted electric field for the pth UC is [47]:

$$\psi(x_P, y_P) = -k_0 x_P \sin\theta_0 \cos\varphi_0 - k_0 y_P \sin\theta_0 \sin\varphi_0 \quad (4)$$

where (x_P, y_P) is the coordinate of the pth UC and k_0 is the free space wavenumbers. The phase of the transmitted electric field of pth UC can be calculated by summing the phase of the incident electric field and the transmission phase shift of the UC [47]:

$$\psi(x_P, y_P) = -k_0 d_P + \psi_n(x_P, y_P) \quad (5)$$

where d_P is the distance between the feed point having the coordinates (x_f, y_f, z_f) and the corresponding planar TA surface point having the coordinates (x_P, y_P, z_P) [47]:

$$d_P = \sqrt{(x_P - x_f)^2 + (y_P - y_f)^2 + (z_P - z_f)^2} \quad (6)$$

Finally, the required phase shift ψ_n for the generic UC of the planar TA, located at (x_P, y_P, z_P), can be calculated from the Equations (4) and (5) [48]:

$$\psi_n = k_0(d_P - (x_P \sin\theta_0 \cos\varphi_0 + y_P \sin\theta_0 \sin\varphi_0)) \quad (7)$$

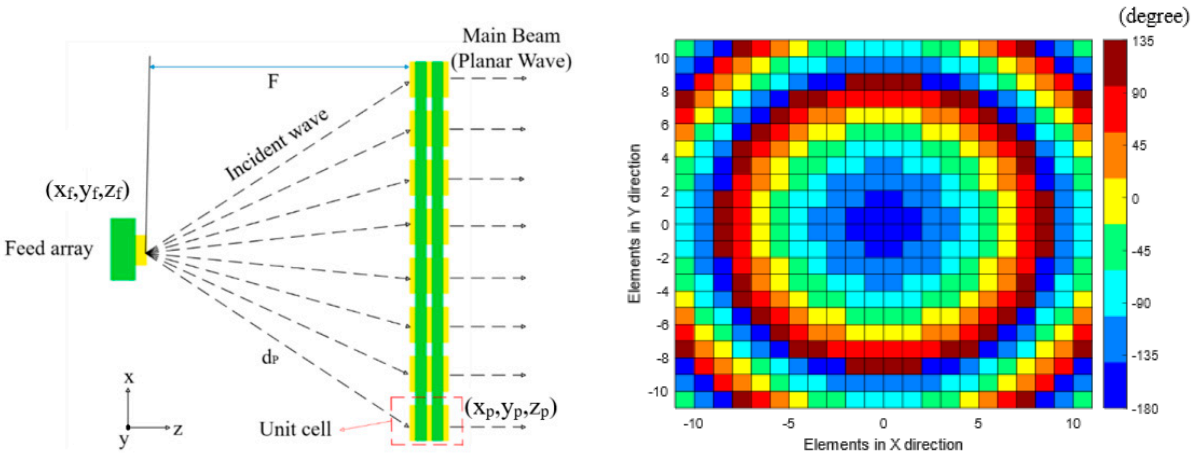

(**a**) (**b**)

Figure 9. (**a**) Ray transmission through TA; (**b**) phase compensation obtained at f_0 = 12 GHz for focal distance F to diameter D ratio of 0.6.

The 3-bit phase compensation can be quantified by the expression (8):

$$\psi_n = \begin{cases} 0^\circ,\ 0^\circ \le \psi_n < 45^\circ \\ 45^\circ,\ 45^\circ \le \psi_n < 90^\circ \\ 90^\circ,\ 90^\circ \le \psi_n < 135^\circ \\ 135^\circ,\ 135^\circ \le \psi_n < 180^\circ \\ 180^\circ,\ 180^\circ \le \psi_n < 225^\circ \\ 225^\circ,\ 225^\circ \le \psi_n < 270^\circ \\ 270^\circ,\ 270^\circ \le \psi_n < 315^\circ \\ 315^\circ,\ 315^\circ \le \psi_n < 360^\circ \end{cases} \quad (8)$$

A home-made software is used to calculate the 3-bit phase distribution of the TA for a focal distance of F = 114.18 mm. The phase compensation required for the broadside pointing direction (θ_0, φ_0) = (0°, 0°) is illustrated in Figure 9b. The distinct colors indicate UCs with different transmission phases; see the colorimetric scale.

5. Simulation and Experimental Results of the TA Antenna

The TA design outlined above does not take in account the feed's primary pattern, the phase discretization, transmission losses, or mutual coupling of the UC. To accurately assess these effects, full wave simulations with CST have been carried out. We fabricated and characterized the TA. Figure 10 presents the fabricated prototype and anechoic chamber measurement, with results compared to simulations. Figure 11 shows the simulated and measured peak gain of the feed antenna without TA and with TA conditions along with the measured aperture efficiency. It is observed from Figure 11 that the simulated realized peak gain is G_{s0} = 23.35 dB, whereas measured peak gain is G_{m0} = 21 dB at f_0 = 12 GHz. At f_1 = 12.4 GHz, the peak gain of this TA for simulation and measurement are G_{s1} = 22.46 dB and G_{m1} = 19.97 dB, respectively. The highest aperture efficiency is η_{max} = 19% at f_2 = 11.2 GHz, whereas it is η_0 = 17% and η_1 = 13% for f_0 = 12 GHz and f_1 = 12.4 GHz, respectively. It is observed that the 1 dB gain bandwidth is BW_g = 10.8% (11.1–12.4 GHz). Figures 12 and 13 show the radiation pattern at f_0 = 12 GHz and f_1 = 12.4 GHz, respectively for E and H plane. The measured peak gains at f_0 = 12 GHz and f_1 = 12.4 GHz are $\triangle G_0$ = 2.35 dB and $\triangle G_1$ = 2.03 dB, less than the simulated gain for both E and H plane, respectively. This difference can be ascribed to larger insertion loss, due

to thin air layer in between the substrates that have not been bonded together with prepreg, and other fabrication tolerances. The measured peak side lobe levels are $SLL_0 = -20.8$ dB and $SLL_1 = -18.5$ dB for $f_0 = 12$ GHz and $f_1 = 12.4$ GHz, respectively.

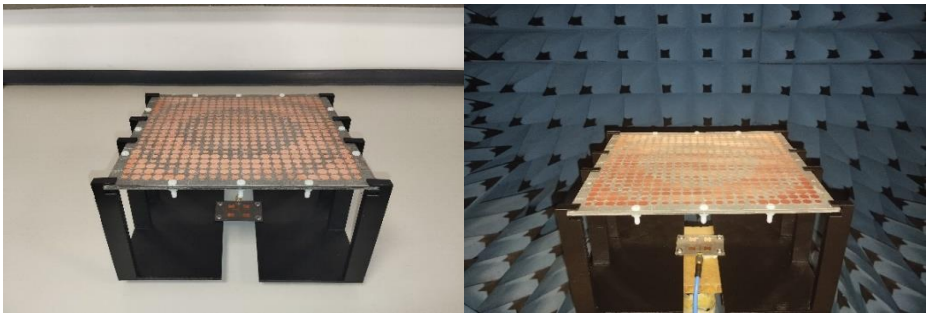

(**a**) (**b**)

Figure 10. (**a**) Fabricated prototype with a support structure; (**b**) measurement setup in anechoic chamber.

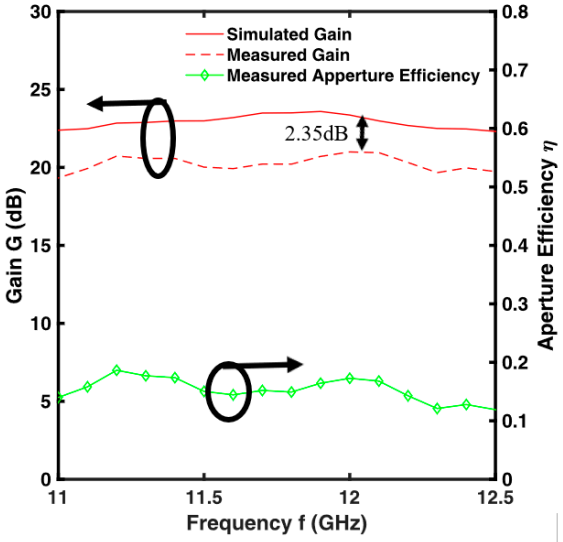

Figure 11. Simulated and measured maximum gain and measured aperture efficiency of TA antenna.

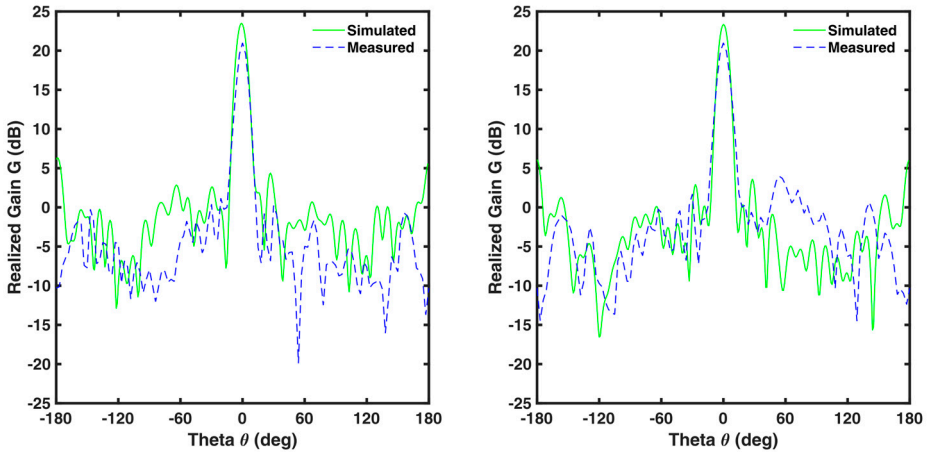

(**a**) (**b**)

Figure 12. Simulated and measured realized gain of TA antenna at $f_0 = 12$ GHz. (**a**) E plane; (**b**) H plane.

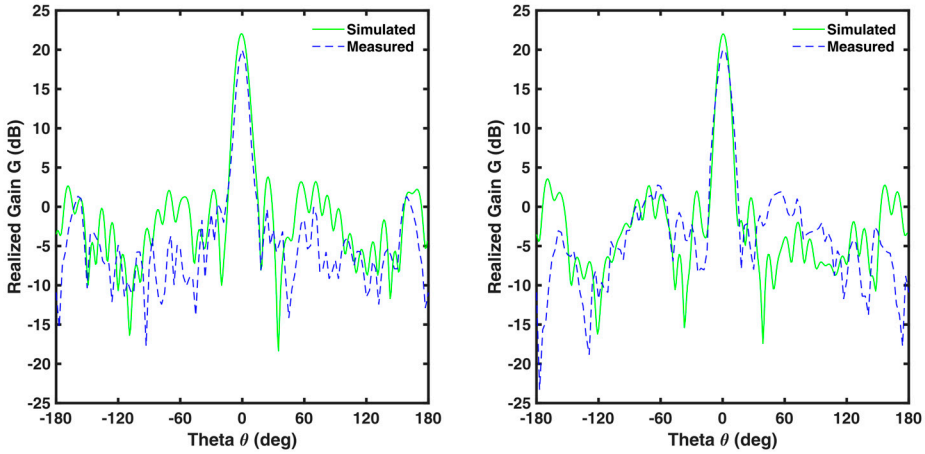

Figure 13. Comparison between simulated and measured realized gain of TA antenna f_1 = 12.4 GHz. (**a**) E plane; (**b**) H plane.

To evaluate the effects of the fabrication tolerances, several simulations have been performed. In particular, all the optimized cells have been slightly changed, by considering an increase of external radius values ΔR_1 = 7.5 µm and a decrease of internal radius values $\Delta R_2 = -7.5$ µm, the obtained gain variation in broadside direction is $\Delta G_{s0} = -0.5$ dB. Moreover, the displacement of the focal distance F of the feed antenna along the z direction has been varied. For a variation of $\Delta F = \pm 4$ mm, the maximum gain is reduced of $G_{s0} = -0.3$ dB and the main beam direction tilts of about $\Delta\theta = -1^\circ$. It is worth noting that, in the design, the substrates are considered perfectly adherent. Since in the prototype fabrication they were assembled with teflon screws, the influence of an air-gap with a thickness t_a = 50 µm between substrates in the unit cell has been investigated, obtaining a transmission coefficient variation $\Delta S_{2,1} = -0.12$ dB and phase shifting variation of $\Delta\phi = 1.3^\circ$ with a gain variation in broadside direction of approximately $\Delta G_{s0} = -0.6$ dB. The employed LPKF Protolaser U3, ultraviolet laser writing equipment, allows a very good fabrication tolerance, providing a scanning beam resolution SBR = 2 µm. As result of the conducted investigation, the reproducibility can be increased by considering a prepreg sheet to assemble the substrates and a more precise mechanical positioner of the feed antenna.

However, as reported in [49–52], low profile TAs can suffer from limited aperture efficiency. Moreover, the unmodeled fabrication imperfections can be the factors that contribute to the low measured aperture efficiency. Optimization strategies such as UC geometry refinement for improved amplitude–phase balance can be employed to improve aperture efficiency by reducing loss mechanisms.

The beam-steering performance of the TA is investigated by moving the SIW-based 2 × 2 patch array feed antenna. The feed antenna is shifted along the *x*-axis (axis shown in Figure 9a) by a feed shifting length (FSL) of 65 mm in both positive and negative directions. The farfield gain patterns for the feed coordinates (x, y) = (0 mm, 0 mm); (x, y) = (+26 mm, 0 mm); (x, y) = (+45 mm, 0 mm); (x, y) = (+65 mm, 0 mm); (x, y) = (−26 mm, 0 mm); (x, y) = (−45 mm, 0 mm); (x, y) = (−65 mm, 0 mm) are plotted in Figures 14 and 15 for f_0 = 12 GHz and f_1 = 12.4 GHz, respectively. The qualitative agreement between the simulated and measured patterns is excellent. The beam-steering angles $\gamma_{max} = \pm 30^\circ$, $\gamma_2 = \pm 20^\circ$, and $\gamma_1 = \pm 11^\circ$ are achieved.

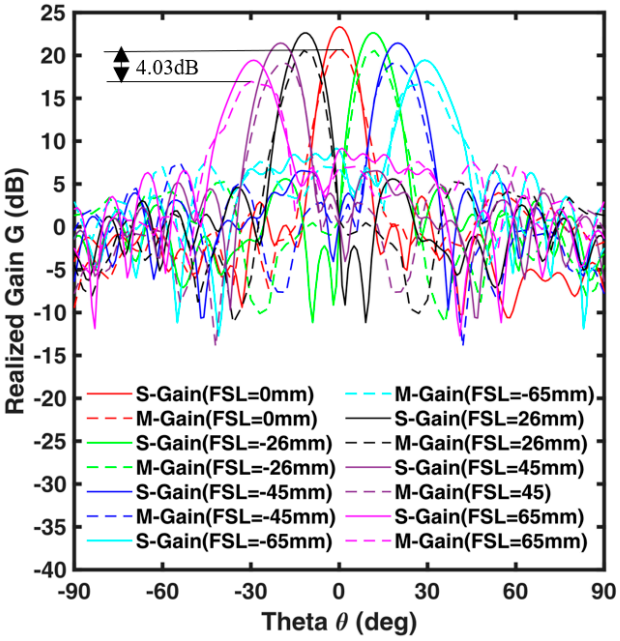

Figure 14. Simulated (solid lines) and measured (dashed lines) beam-steering performance at f_0 = 12 GHz.

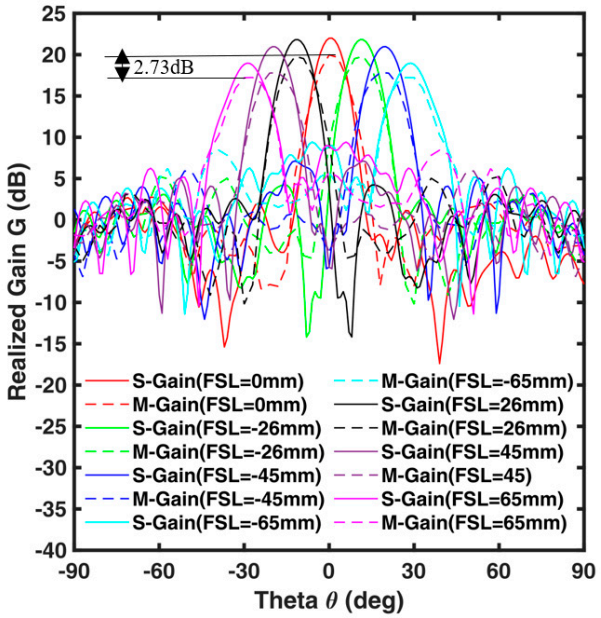

Figure 15. Simulated (solid lines) and measured (dashed lines) beam-steering performance at f_1 = 12.4 GHz.

However, in every case, the measured gain is slightly lower than the simulated one, as previously observed and discussed for the broadside pointing direction. Again, this discrepancy may be attributed to fabrication errors. As example, the width of the circular ring in some UCs is R_1–R_2 = 0.1 mm, a width requiring tight tolerances. For $\gamma_{max} = \pm 30^\circ$ beam steering the simulated scan loss is $\triangle G_{SSL0}$ = 3.9 dB at f_0 = 12 GHz and $\triangle G_{SSL1}$ = 3.03 dB at f_1 = 12.4 GHz. In measurement, it is observed that for $\gamma_{max} = \pm 30^\circ$ steering, the scan loss is $\triangle G_{MSL0}$ = 4.03 dB at f_0 = 12 GHz and $\triangle G_{MSL1}$ = 2.73 dB at f_1 = 12.4 GHz. Moreover, in the experiment, the actual position of the feed antenna during beam steering operation is slightly different with respect to the simulated one, this resulting in a lower measured gain with respect to the simulation. Also, the air gap between the substrates which is not considered during simulation causes a mismatch between the simulated and the measured

scan loss. It can be concluded that the TA at f_0 = 12 GHz outperforms the same at for gain increment but in the case of beam steering it shows better performance at in terms of scan loss △G. The measurement is done by shifting the feed antenna only along the x axis. Similar results are obtained by shifting the feed antenna along the y axis due to the symmetrical nature of this TA.

Though the mechanical feed displacement for beam steering works well in this case, it is not feasible for some applications. Future work will explore the integration of reconfigurable elements, such as varactor diodes or tunable materials, within the UC architecture for beam steering to overcome the limitations associated with mechanical feed displacement. Dynamic phase control across the aperture is necessary for electronic beam steering, which can be employed by incorporating electronically tunable components. Furthermore, this advancement will allow better control of polarization, adaptive beam shaping, and multi-beam operation in real-world applications.

6. Comparison with Other Works

The performance of this proposed TA is compared with some related work listed in Table 4. It is observed that the proposed TA has a lower profile, having thickness $\rho = 0.126\lambda_0$ [49–52]. It consists of three layers with a reduced array size of $A = 57.9\lambda_0^2$ [49,51,53]. This proposed TA does not require an air gap in between the substrates, offering improved robustness, compactness, and ease of fabrication. Moreover, the low F/D = 0.6 makes this TA more compact than [51,52]. Moreover, the 8-phase state having less than α_T = 1.3 dB transmission loss with dual linear polarized components transmission capability is not achieved in [49,50,53]. For the case of beam steering, the proposed TA can scan $\gamma_{max} = \pm 30°$, which is greater than [49,53]. This work achieves the lowest scan loss among the reference works of $\triangle G_{MSL1}$ = 2.73 dB at f_1 = 12.4 GHz [49–53]. However, the aperture efficiency η is not better in comparison with the reference papers reported in Table 4 except [53]. It can be concluded that the lower profile is achieved at the cost of aperture efficiency η or gain G.

Table 4. Comparison of proposed TA with other works.

Ref.	Jiang et al., 2017 [49]	Zhang et al., 2020 [50]	Niroo Jazi et al., 2016 [51]	Li et al., 2021 [52]	Li et al., 2021 [53]	This Work	
Frequency f (GHz)	27.5	10	12	15	12.5	12	12.4
No. of layers	2	3	5	3	3	3	3
Thickness ρ (λ_0)	0.18	0.133	0.582	0.165	0.083	0.126	0.13
Array size A (λ_0^2)	86.06	16.0	64.0	38.48	90.9	57.9	62.35
Gain G (dB)	24.2	19.3	23.0	23.06	22.7	21.0	19.97
Scan range γ_{max} (degree)	±27	+60	±35	±30	±21	±30	±30
Scan loss △G (dB)	3.7	4.15	3.0	3.6	2.7	4.03	2.73
F/D	0.50	0.60	0.78	0.75	0.59	0.60	0.60
Polarization	Dual LP	Single CP	Ins. *	Dual LP and Dual CP	Single LP	Dual LP	Dual LP
Side Lobe Level SLL (dB)	−18.4	−17.7	−15.0	−35.0	−15.0	−20.8	−18.5
Phase states	240°	180°	360°	360°	360°	360°	360°
Air gap	Yes	No	No	Yes	No	No	No
Aperture Efficiency η (%)	24.5	40.2	34.64	42.3	15.2	17.0	13.0

* Ins. = Insensitive.

Therefore, by considering all the factors, the proposed transmitarray can be considered (i) novel (metal patterns with circular geometry), (ii) low profile (to parity of performance),

(iii) dual-polarized, (iv) simple to be fabricated, (v) with good scan loss at 12.4 GHz and (vi) with good steering angle.

7. Conclusions

A low profile, dual-polarized 3-bit TA is proposed, simulated, and tested in this research. This proposed TA achieves a low profile ($0.126\lambda_0$), dual-polarized operation, and efficient beam steering up to $\pm 30^\circ$ with minimal scan loss, with a 1 dB gain bandwidth of BW_g = 10.8% (11.1–12.4 GHz), and a measured peak side lobe level $SLL_1 = -20.8$ dB at f_0 = 12 GHz. In particular, a measured scan loss of $\triangle G_{MSL0}$ = 4.03 dB and $\triangle G_{MSL1}$ = 2.73 dB is achieved at f_0 = 12 GHz and f_1 = 12.4 GHz, respectively. The measured peak gain is G_{m0} = 21 dB at f_0 = 12 GHz with an aperture efficiency of η_0 = 17% at whereas the maximum aperture efficiency is η_{max} = 19% found at f_2 = 11.2 GHz. All these features make this TA suitable for Ku-band satellite and 5G applications.

Author Contributions: Conceptualization, investigation, and methodology, M.I.K., A.M.L., F.A., V.V.F., A.U.K., M.S., G.S. and F.P.; writing—original draft preparation, M.I.K.; writing—review and editing, M.I.K., A.M.L., F.A., G.S. and F.P.; supervision, F.P.; funding acquisition, F.P. All authors have read and agreed to the published version of the manuscript.

Funding: This work was partially supported by MIUR PRIN 2022, NRPP–DD n. 1181 del 27-07-2023—Innovative technologies for non-invasive assessment of plant health condition to support precision farming "VEGETATION" (P2022ZF9P2, CUP: I53D23005710 001); H2020-ICT-37-2020 "Photonic Accurate and Portable Sensor Systems Exploiting Photo-Acoustic and PhotoThermal Based Spectroscopy for Real-Time Outdoor Air Pollution Monitoring—PASSEPARTOUT" n. 101016956; the European Union under the Italian National Recovery and Resilience Plan (NRRP) of NextGenerationEU, with reference to the partnership on "Telecommunications of the Future" (PE00000001—program "RESTART", CUP: D93C22000910001)—STRUCTURAL PROJECT Antennas & Devices for mixing, detection And Manipulation of mmWaves; ASI 687/2022—MUR 341 15/03/22 "SPACE IT UP" (CUP: D53C24000570006); ASI 2024-68-I.0 "Origami Reconfigurable Beam-steering Antennas with METAsurfaces for Communication on Small Satellites—ORBIT-META" (CUP: F93C24000550001); and HORIZON TMA MSCA Staff Exchanges (101182995) "Cr4+:YAG/Polymer nanocomposite as alternative materials for Q-switched lasers: properties, modeling, and applications—ALTER-Q".

Institutional Review Board Statement: Not applicable.

Informed Consent Statement: Not applicable.

Data Availability Statement: Data is contained within the article.

Conflicts of Interest: The authors declare no conflicts of interest.

Abbreviations

The following abbreviations are used in this manuscript:

TA	Transmitarray
UC	Unit cell
ECM	Equivalent circuit model

References

1. Alhalabi, R.A.; Rebeiz, G.M. High-efficiency angled-dipole antennas for millimeter-wave phased array applications. *IEEE Trans. Antennas Propag.* **2008**, *56*, 3136–3142. [CrossRef]
2. Zhang, H.Y.; Zhang, F.S.; Zhang, F.; Sun, F.K.; Xie, G.J. High-power array antenna based on phase-adjustable array element for wireless power transmission. *IEEE Antennas Wirel. Propag. Lett.* **2017**, *16*, 2249–2253. [CrossRef]
3. Zhang, S.; Chen, X.; Syrytsin, I.; Pedersen, G.F. A planar switchable 3-D-coverage phased array antenna and its user effects for 28-GHz mobile terminal applications. *IEEE Trans. Antennas Propag.* **2017**, *65*, 6413–6421. [CrossRef]

4. Han, G.; Du, B.; Wu, W.; Yang, B. A novel hybrid phased array antenna for satellite communication on-the-move in Ku-band. *IEEE Trans. Antennas Propag.* **2015**, *63*, 1375–1383. [CrossRef]
5. Wang, Z.; Zhang, G.X.; Yin, Y.; Wu, J. Design of a dual-band high-gain antenna array for WLAN and WiMAX base station. *IEEE Antennas Wirel. Propag. Lett.* **2014**, *13*, 1721–1724. [CrossRef]
6. Alotaibi, N.N.; Hamdi, K.A. Switched phased-array transmission architecture for secure millimeter-wave wireless communication. *IEEE Trans. Commun.* **2016**, *64*, 1303–1312. [CrossRef]
7. Hwang, S.; Lee, B.; Kim, D.H.; Park, J.Y. Design of S-band phased array antenna with high isolation using broadside coupled split ring resonator. *J. Electromagn. Eng. Sci.* **2018**, *18*, 108–116. [CrossRef]
8. Xu, H.X.; Cai, T.; Zhuang, Y.Q.; Peng, Q.; Wang, G.; Liang, J.G. Dual-mode transmissive metasurface and its applications in multibeam transmitarray. *IEEE Trans. Antennas Propag.* **2017**, *65*, 1797–1806. [CrossRef]
9. Diaby, F.; Clemente, A.; Sauleau, R.; Pham, K.T.; Dussopt, L. 2-bit reconfigurable unit-cell and electronically steerable transmitarray at Ka-band. *IEEE Trans. Antennas Propag.* **2020**, *68*, 5003–5008. [CrossRef]
10. Wang, Y.; Xu, S.; Yang, F.; Li, M. A novel 1-bit wide-angle beam scanning reconfigurable transmitarray antenna using an equivalent magnetic dipole element. *IEEE Trans. Antennas Propag.* **2020**, *68*, 5691–5695. [CrossRef]
11. Zeng, Q.; Xue, Z.; Ren, W.; Li, W. Dual-band beam-scanning antenna using rotatable planar phase gradient transmitarrays. *IEEE Trans. Antennas Propag.* **2020**, *68*, 5021–5026. [CrossRef]
12. Liang, Z.; Ouyang, J.; Yang, F. Low-profile wideband circularly polarised single-layer metasurface antenna. *Electron. Lett.* **2018**, *54*, 1362–1364. [CrossRef]
13. Abdelrahman, A.H.; Nayeri, P.; Elsherbeni, A.Z.; Yang, F. Single-feed quad-beam transmitarray antenna design. *IEEE Trans. Antennas Propag.* **2016**, *64*, 953–959. [CrossRef]
14. Zheng, B.; Fan, Y.; Cheng, Y.J. Wideband high-efficiency circularly polarized transmitarray with linearly polarized feed. *IEEE Antennas Wirel. Propag. Lett.* **2023**, *22*, 1451–1455. [CrossRef]
15. Abdelrahman, A.H.; Yang, F.; Elsherbeni, A.Z.; Nayeri, P.; Balanis, C.A. *Analysis and Design of Transmitarray Antennas*; Springer: Cham, Switzerland, 2017; pp. 1–151.
16. Ramazannia Tuloti, S.H.; Rezaei, P.; Tavakkol Hamedani, F. High-efficient wideband transmitarray antenna. *IEEE Antennas Wirel. Propag. Lett.* **2018**, *17*, 817–820. [CrossRef]
17. Watts, C.M.; Pedross-Engel, A.; Smith, D.R.; Reynolds, M.S. X-band SAR imaging with a liquid-crystal-based dynamic metasurface antenna. *J. Opt. Soc. Am. B Opt. Phys.* **2017**, *34*, 300–306. [CrossRef]
18. Arbabi, E.; Arbabi, A.; Kamali, S.M.; Horie, Y.; Faraji-Dana, M.; Faraon, A. MEMS-tunable dielectric metasurface lens. *Nat. Commun.* **2018**, *9*, 812. [CrossRef] [PubMed]
19. Sleasman, T.; Imani, M.F.; Xu, W.; Hunt, J.; Driscoll, T.; Reynolds, M.S.; Smith, D.R. Waveguide-fed tunable metamaterial element for dynamic apertures. *IEEE Antennas Wirel. Propag. Lett.* **2016**, *15*, 606–609. [CrossRef]
20. Xu, H.-X.; Tang, S.; Ma, S.; Luo, W.; Cai, T.; Sun, S.; He, Q.; Zhou, L. Tunable microwave metasurfaces for high-performance operations: Dispersion compensation and dynamical switch. *Sci. Rep.* **2016**, *6*, 38255. [CrossRef]
21. Massaccesi, A.; Dassano, G.; Pirinoli, P. Beam scanning capabilities of a 3D-printed perforated dielectric transmitarray. *Electronics* **2019**, *8*, 379. [CrossRef]
22. Ali, Q.; Shahzad, W.; Ahmad, I.; Safiq, S.; Bin, X.; Abbas, S.M.; Sun, H. Recent developments and challenges on beam steering characteristics of reconfigurable transmitarray antennas. *Electronics* **2022**, *11*, 587. [CrossRef]
23. Lee, J.-G.; Kwon, T.-S.; Lee, J.-H. Beam pattern reconfigurable circularly polarized transmitarray antenna by rearrangement of sources. *Microw. Opt. Technol. Lett.* **2019**, *61*, 999–1003. [CrossRef]
24. Lee, C.; Hoang, T.V.; Wook, S.; Lee, S.; Lee, J. Low-profile quad-beam circularly polarised antenna using transmissive metasurface. *IET Microw. Antennas Propag.* **2019**, *13*, 1690–1698. [CrossRef]
25. Mei, P.; Zhang, S.; Pedersen, G.F. A low-profile and beam-steerable transmitarray antenna: Design, fabrication, and measurement [Antenna Applications Corner]. *IEEE Antennas Propag. Mag.* **2021**, *63*, 88–101. [CrossRef]
26. De Marco, R.; Arnieri, E.; Greco, F.; Bordbar, A.; Amendola, G.; Boccia, L. Low-profile dual-band dual-polarized transmitarray antenna based on multilayer frequency selective surfaces. *IEEE Trans. Antennas Propag.* **2023**, *71*, 7354–7362. [CrossRef]
27. Jiao, X.-H.; Wan, G. A novel low-profile planar microstrip transmitarray antenna with high efficiency. *Int. J. RF Microw. Comput.-Aided Eng.* **2021**, *31*, e22614. [CrossRef]
28. Park, J.-H.; Lee, J.-G. Low-profile high-efficiency transmitarray antenna using optimized phase compensation surface (PCS) and PEC sidewalls. *ICT Express* **2021**, *7*, 501–506. [CrossRef]
29. Frank, M.; Lurz, F.; Weigel, R.; Koelpin, A. Low-profile and low-cost transmitarray antenna at 122 GHz based on unit-cells with 1-bit phase resolution. *Electron. Lett.* **2020**, *56*, 1293–1295. [CrossRef]
30. Wang, X.; Cheng, Y.; Dong, Y. Millimeter-wave high-efficiency double-layer transmitarray antenna using miniaturized dual-polarized elements. *IEEE Trans. Antennas Propag.* **2022**, *70*, 8637–8642. [CrossRef]

31. Li, T.; Sun, J.; Meng, H.; Shen, Y.; Hu, S.; Dou, W.; Chen, Z.N.; Zwick, T. Characteristic mode inspired dual-polarized double-layer metasurface lens. *IEEE Trans. Antennas Propag.* **2021**, *69*, 3144–3154. [CrossRef]
32. Xue, C.; Sun, J.; Niu, L.; Lou, Q. Ultrathin dual-polarized Huygens' metasurface: Design and application. *Ann. Phys.* **2020**, *532*, 2000151. [CrossRef]
33. Yang, S.; Yan, Z.; Cai, M.; Fan, F.; Zhang, T. A high-efficiency double-layer transmitarray antenna using low-loss dual-linearly polarized elements. *IEEE Antennas Wirel. Propag. Lett.* **2020**, *19*, 2378–2382. [CrossRef]
34. Yi, X.; Su, T.; Li, X.; Wu, B.; Yang, L. A double-layer wideband transmitarray antenna using two degrees of freedom elements around 20 GHz. *IEEE Trans. Antennas Propag.* **2019**, *67*, 2798–2802. [CrossRef]
35. Pham, K.; Nguyen, N.T.; Clemente, A.; Di Palma, L.; Le Coq, L.; Dussopt, L.; Sauleau, R. Design of wideband dual linearly polarized transmitarray antennas. *IEEE Trans. Antennas Propag.* **2016**, *64*, 2022–2026. [CrossRef]
36. Aziz, A.; Yang, F.; Xu, S.; Li, M. An efficient dual-band orthogonally polarized transmitarray design using three-dipole elements. *IEEE Antennas Wirel. Propag. Lett.* **2018**, *17*, 319–322. [CrossRef]
37. Bagheri, M.O.; Hassani, H.R.; Rahmati, B. Dual-band, dual-polarised metallic slot transmitarray antenna. *IET Microw. Antennas Propag.* **2017**, *11*, 402–409. [CrossRef]
38. Aziz, A.; Yang, F.; Xu, S.; Li, M.; Chen, H.-T. A high-gain dual-band and dual-polarized transmitarray using novel loop elements. *IEEE Antennas Wirel. Propag. Lett.* **2019**, *18*, 1213–1217. [CrossRef]
39. Wu, F.; Wang, J.; Xiang, L.; Hong, W.; Luk, K.-M. A wideband dual-polarized magneto-electric dipole transmitarray with independent control of polarizations. *IEEE Trans. Antennas Propag.* **2022**, *70*, 8632–8636. [CrossRef]
40. Pham, K.T.; Sauleau, R.; Fourn, E.; Diaby, F.; Clemente, A.; Dussopt, L. Dual-band transmitarrays with dual-linear polarization at Ka-band. *IEEE Trans. Antennas Propag.* **2017**, *65*, 7009–7018. [CrossRef]
41. Pan, W.; Huang, C.; Ma, X.; Jiang, B.; Luo, X. A dual linearly polarized transmitarray element with 1-bit phase resolution in X-band. *IEEE Antennas Wirel. Propag. Lett.* **2015**, *14*, 167–170. [CrossRef]
42. Saleh, W.; Letestu, Y.; Sauleau, R.; Cruz, E.M. Design and measurements of a high-performance wideband transmitarray antenna for D-band communications. *IEEE Antennas Wirel. Propag. Lett.* **2021**, *20*, 1765–1769. [CrossRef]
43. Wang, Y.; Xu, S.; Yang, F.; Werner, D.H. 1-bit dual-linear polarized reconfigurable transmitarray antenna using asymmetric dipole elements with parasitic bypass dipoles. *IEEE Trans. Antennas Propag.* **2021**, *69*, 1188–1192. [CrossRef]
44. Zhang, S.; Cao, W.; Wu, T.; Wang, J.; Wei, Y. The Design of a Multifunctional Coding Transmitarray with Independent Manipulation of the Polarization States. *Micromachines* **2024**, *15*, 1014. [CrossRef] [PubMed]
45. Li, Z.; Weng, X.; Yi, X.; Li, K.; Duan, W.; Bi, M. Design and analysis of a complementary structure-based high selectivity tri-band frequency selective surface. *Sci. Rep.* **2024**, *14*, 9415. [CrossRef]
46. Losito, O.; Portosi, V.; Venanzoni, G.; Bigelli, F.; Mencarelli, D.; Scalmati, P.; Renghini, C.; Carta, P.; Prudenzano, F. Feasibility investigation of SIW cavity-backed patch antenna array for Ku-band applications. *Appl. Sci.* **2019**, *9*, 1271. [CrossRef]
47. Huang, G.-L.; Pang, Z.-Y.; Al-Nuaimi, M.K.T.; Kishk, A.A.; Mahmoud, A. A Broadband and High-Aperture-Efficiency Multilayer Transmitarray Based on Aperture-Coupled Slot Unit Cells. *IEEE Trans. Antennas Propag.* **2023**, *71*, 9633–9642. [CrossRef]
48. Fan, Y.-L.; Lin, X.-Q.; Liu, S.-L. A broadband bifocal conformal transmitarray antenna with wide scanning angles. *Microw. Opt. Technol. Lett.* **2022**, *64*, 1800–1808. [CrossRef]
49. Jiang, M.; Chen, Z.N.; Zhang, Y.; Hong, W.; Xuan, X. Metamaterial-based thin planar lens antenna for spatial beamforming and multibeam massive MIMO. *IEEE Trans. Antennas Propag.* **2017**, *65*, 464–472. [CrossRef]
50. Zhang, F.; Yang, G.-M.; Jin, Y.-Q. Low-Profile Circularly Polarized Transmitarray for Wide-Angle Beam Control With a Third-Order Meta-FSS. *IEEE Trans. Antennas Propag.* **2020**, *68*, 3586–3597. [CrossRef]
51. Niroo Jazi, M.; Chaharmir, M.R.; Shaker, J.; Sebak, A.R. Broadband transmitarray antenna design using polarization-insensitive frequency selective surfaces. *IEEE Trans. Antennas Propag.* **2016**, *64*, 99–108. [CrossRef]
52. Li, M.-Y.; Ban, Y.-L.; Yan, F.-Q. Wideband low-profile Ku-band transmitarray antenna. *IEEE Access* **2021**, *9*, 6683–6688. [CrossRef]
53. Li, G.; Ge, Y.; Chen, Z. A compact multibeam folded transmitarray antenna at Ku-band. *IEEE Antennas Wirel. Propag. Lett.* **2021**, *20*, 808–812. [CrossRef]